



HAL
open science

Predicting minimum uncertainties in the inversion of ocean color geophysical parameters based on Cramer-Rao bounds

Sylvain Jay, Mireille Guillaume, Malik Chami, Audrey Minghelli, Yannick
Deville, Bruno Lafrance, Véronique Serfaty

► To cite this version:

Sylvain Jay, Mireille Guillaume, Malik Chami, Audrey Minghelli, Yannick Deville, et al.. Predicting minimum uncertainties in the inversion of ocean color geophysical parameters based on Cramer-Rao bounds. *Optics Express*, 2018, 26 (2), pp.A1-A18. 10.1364/OE.26.0000A1 . insu-01671185

HAL Id: insu-01671185

<https://insu.hal.science/insu-01671185>

Submitted on 22 Dec 2017

HAL is a multi-disciplinary open access archive for the deposit and dissemination of scientific research documents, whether they are published or not. The documents may come from teaching and research institutions in France or abroad, or from public or private research centers.

L'archive ouverte pluridisciplinaire **HAL**, est destinée au dépôt et à la diffusion de documents scientifiques de niveau recherche, publiés ou non, émanant des établissements d'enseignement et de recherche français ou étrangers, des laboratoires publics ou privés.



Predicting minimum uncertainties in the inversion of ocean color geophysical parameters based on Cramer-Rao bounds

SYLVAIN JAY,^{1,*} MIREILLE GUILLAUME,¹ MALIK CHAMI,^{2,3} AUDREY MINGHELLI,⁴ YANNICK DEVILLE,⁵ BRUNO LAFRANCE,⁶ AND VÉRONIQUE SERFATY⁷

¹Aix Marseille Univ, CNRS, Centrale Marseille, Institut Fresnel, F-13013 Marseille, France

²Sorbonne Universités, UPMC Univ Paris 06, INSU-CNRS, Laboratoire Atmosphères Milieux Observations Spatiales (LATMOS), 06230 Villefranche sur Mer, France

³Institut Universitaire de France, 75231 Paris Cedex 05, France

⁴University of Toulon, CNRS, SeaTech, LSIS laboratory, UMR 7296, 83041 Toulon, France

⁵Institut de Recherche en Astrophysique et Planétologie (IRAP), Observatoire Midi-Pyrénées, Université de Toulouse, UPS-CNRS-OMP, 31400 Toulouse, France

⁶CS Systemes d'Information, 31506 Toulouse Cedex 05, France

⁷DGA/DS/MRIS, 75509 Paris Cedex 15, France

*sylvain.jay@fresnel.fr

Abstract: We present an analytical approach based on Cramer-Rao Bounds (CRBs) to investigate the uncertainties in estimated ocean color parameters resulting from the propagation of uncertainties in the bio-optical reflectance modeling through the inversion process. Based on given bio-optical and noise probabilistic models, CRBs can be computed efficiently for any set of ocean color parameters and any sensor configuration, directly providing the minimum estimation variance that can be possibly attained by any unbiased estimator of any targeted parameter. Here, CRBs are explicitly developed using (1) two water reflectance models corresponding to deep and shallow waters, resp., and (2) four probabilistic models describing the environmental noises observed within four Sentinel-2 MSI, HICO, Sentinel-3 OLCI and MODIS images, resp. For both deep and shallow waters, CRBs are shown to be consistent with the experimental estimation variances obtained using two published remote-sensing methods, while not requiring one to perform any inversion. CRBs are also used to investigate to what extent perfect *a priori* knowledge on one or several geophysical parameters can improve the estimation of remaining unknown parameters. For example, using pre-existing knowledge of bathymetry (e.g., derived from LiDAR) within the inversion is shown to greatly improve the retrieval of bottom cover for shallow waters. Finally, CRBs are shown to provide valuable information on the best estimation performances that may be achieved with the MSI, HICO, OLCI and MODIS configurations for a variety of oceanic, coastal and inland waters. CRBs are thus demonstrated to be an informative and efficient tool to characterize minimum uncertainties in inverted ocean color geophysical parameters.

© 2017 Optical Society of America

OCIS codes: (010.4450) Oceanic optics; (100.3190) Inverse problems; (110.4234) Multispectral and hyperspectral imaging; (280.0280) Remote sensing and sensors.

References and links

1. P. J. Werdell, B. A. Franz, S. W. Bailey, G. C. Feldman, E. Boss, V. E. Brando, M. Dowell, T. Hirata, S. J. Lavender, Z. Lee, H. Loisel, S. Maritorea, F. Mélin, T. S. Moore, T. J. Smyth, D. Antoine, E. Devred, O. H. F. D'Andon, and A. Mangin, "Generalized ocean color inversion model for retrieving marine inherent optical properties," *Appl. Opt.* **52**, 2019–2037 (2013).
2. J. D. Hedley, C. M. Roelfsema, I. Chollett, A. R. Harborne, S. F. Heron, S. J. Weeks, W. J. Skirving, A. E. Strong, C. M. Eakin, T. R. Christensen, V. Ticzon, S. Bejarano, and P. J. Mumby, "Remote sensing of coral reefs for monitoring and management: A review," *Remote Sens.* **8**, 118 (2016).
3. R. A. Garcia, P. R. Fearn, and L. I. McKinna, "Detecting trend and seasonal changes in bathymetry derived from HICO imagery: A case study of Shark Bay, Western Australia," *Remote Sens. Environ.* **147**, 186–205 (2014).

4. T. S. Moore, J. W. Campbell, and M. D. Dowell, "A class-based approach to characterizing and mapping the uncertainty of the MODIS ocean chlorophyll product," *Remote Sens. Environ.* **113**, 2424–2430 (2009).
5. M. S. Salama and A. Stein, "Error decomposition and estimation of inherent optical properties," *Appl. Opt.* **48**, 4947–4962 (2009).
6. J. D. Hedley, C. M. Roelfsema, S. R. Phinn, and P. J. Mumby, "Environmental and sensor limitations in optical remote sensing of coral reefs: Implications for monitoring and sensor design," *Remote Sens.* **4**, 271–302 (2012).
7. W. W. Gregg, "Assimilation of SeaWiFS ocean chlorophyll data into a three-dimensional global ocean model," *J. Mar. Syst.* **69**, 205–225 (2008).
8. Z. Lee, R. Arnone, C. Hu, P. J. Werdell, and B. Lubac, "Uncertainties of optical parameters and their propagations in an analytical ocean color inversion algorithm," *Appl. Opt.* **49**, 369–381 (2010).
9. N. Pahlevan, S. Sarkar, and B. A. Franz, "Uncertainties in coastal ocean color products: Impacts of spatial sampling," *Remote Sens. Environ.* **181**, 14–26 (2016).
10. Z. Lee and K. L. Carder, "Effect of spectral band numbers on the retrieval of water column and bottom properties from ocean color data," *Appl. Opt.* **41**, 2191–2201 (2002).
11. P. Wang, E. S. Boss, and C. Roesler, "Uncertainties of inherent optical properties obtained from semianalytical inversions of ocean color," *Appl. Opt.* **44**, 4074–4085 (2005).
12. Z. Lee, A. Weidemann, and R. Arnone, "Combined Effect of reduced band number and increased bandwidth on shallow water remote sensing: The case of Worldview 2," *IEEE Trans. Geosci. Remote Sens.* **51**, 2577–2586 (2013).
13. D. R. Lyzenga, "Passive remote sensing techniques for mapping water depth and bottom features," *Appl. Opt.* **17**, 379–383 (1978).
14. Z. Lee, K. L. Carder, C. D. Mobley, R. G. Steward, and J. S. Patch, "Hyperspectral remote sensing for shallow waters: 2. deriving bottom depths and water properties by optimization," *Appl. Opt.* **38**, 3831–3843 (1999).
15. V. Brando, J. Anstee, M. Wettle, A. Dekker, S. Phinn, and C. Roelfsema, "A physics based retrieval and quality assessment of bathymetry from suboptimal hyperspectral data," *Remote Sens. Environ.* **113**, 755–770 (2009).
16. J. Hedley, C. Roelfsema, and S. R. Phinn, "Efficient radiative transfer model inversion for remote sensing applications," *Remote Sens. Environ.* **113**, 2527–2532 (2009).
17. A. G. Dekker, S. R. Phinn, J. Anstee, P. Bissett, V. E. Brando, B. Casey, P. Fearn, J. Hedley, W. Klonowski, Z. P. Lee, M. Lynch, M. Lyons, C. Mobley, and C. Roelfsema, "Intercomparison of shallow water bathymetry, hydro-optics, and benthos mapping techniques in Australian and Caribbean coastal environments," *Limnol. Oceanogr. Methods* **9**, 396–425 (2011).
18. S. Jay and M. Guillaume, "A novel maximum likelihood based method for mapping depth and water quality from hyperspectral remote-sensing data," *Remote Sens. Environ.* **147**, 121–132 (2014).
19. L. I. McKinna, P. R. Fearn, S. J. Weeks, P. J. Werdell, M. Reichstetter, B. A. Franz, D. M. Shea, and G. C. Feldman, "A semianalytical ocean color inversion algorithm with explicit water column depth and substrate reflectance parameterization," *J. Geophys. Res. Oceans* **120**, 1741–1770 (2015).
20. S. Jay and M. Guillaume, "Regularized estimation of bathymetry and water quality using hyperspectral remote sensing," *Int. J. Remote Sens.* **37**, 263–289 (2016).
21. S. Jay, M. Guillaume, A. Minghelli, Y. Deville, M. Chami, B. Lafrance, and V. Serfaty, "Hyperspectral remote sensing of shallow waters: Considering environmental noise and bottom intra-class variability for modeling and inversion of water reflectance," *Remote Sens. Environ.* **200**, 352–367 (2017).
22. J. E. O'Reilly, S. Maritorena, B. G. Mitchell, D. A. Siegel, K. L. Carder, S. A. Garver, M. Kahru, and C. McClain, "Ocean color chlorophyll algorithms for SeaWiFS," *J. Geophys. Res. Oceans* **103**, 24937–24953 (1998).
23. Z. Lee, K. L. Carder, and R. A. Arnone, "Deriving inherent optical properties from water color: a multiband quasi-analytical algorithm for optically deep waters," *Appl. Opt.* **41**, 5755–5772 (2002).
24. D. B. Gillis, J. H. Bowles, and W. J. Moses, "Improving the retrieval of water inherent optical properties in noisy hyperspectral data through statistical modeling," *Opt. Express* **21**, 21306–21316 (2013).
25. P. H. Garthwaite, I. T. Jolliffe, and B. Jones, *Statistical inference* (Oxford University, 2002).
26. A. Roueff, A. Arnaubec, P. C. Dubois-Fernandez, and P. Refregier, "Cramer-rao lower bound analysis of vegetation height estimation with random volume over ground model and polarimetric sar interferometry," *IEEE Geosci. Remote Sens. Lett.* **8**, 1115–1119 (2011).
27. X. Liu, S. Bourennane, and C. Fossati, "Denoising of hyperspectral images using the PARAFAC model and statistical performance analysis," *IEEE Trans. Geosci. Remote Sens.* **50**, 3717–3724 (2012).
28. S. Jay and M. Guillaume, "Estimation of water column parameters with a maximum likelihood approach," in "3rd Workshop on Hyperspectral Image and Signal Processing: Evolution in Remote Sensing," (IEEE, 2011), pp. 1–4.
29. J. Hedley, C. Roelfsema, B. Koetz, and S. Phinn, "Capability of the Sentinel-2 mission for tropical coral reef mapping and coral bleaching detection," *Remote Sens. Environ.* **120**, 145–155 (2012).
30. R. A. Garcia, L. I. McKinna, J. D. Hedley, and P. R. Fearn, "Improving the optimization solution for a semi-analytical shallow water inversion model in the presence of spectrally correlated noise," *Limnol. Oceanogr. Methods* **12**, 651–669 (2014).
31. V. E. Brando and A. G. Dekker, "Satellite hyperspectral remote sensing for estimating estuarine and coastal water quality," *IEEE Trans. Geosci. Remote Sens.* **41**, 1378–1387 (2003).
32. Z. Lee, K. L. Carder, C. D. Mobley, R. G. Steward, and J. S. Patch, "Hyperspectral remote sensing for shallow waters. i. a semianalytical model," *Appl. Opt.* **37**, 6329–6338 (1998).

33. H. Buiteveld, J. Hakvoort, and M. Donze, "Optical properties of pure water," in "Ocean Optics XII," (International Society for Optics and Photonics, 1994), pp. 174–183.
34. A. Morel, "Optical properties of pure water and pure sea water," *Optical aspects of oceanography* **1**, 1–24 (1974).
35. P. Stoica and R. L. Moses, *Spectral analysis of signals*, vol. 452 (Pearson Prentice Hall Upper Saddle River, NJ, 2005).
36. K. Dörnhöfer, A. Göritz, P. Gege, B. Pflug, and N. Oppelt, "Water constituents and water depth retrieval from Sentinel-2A-A first evaluation in an oligotrophic lake," *Remote Sens.* **8**, 941 (2016).
37. V. S. Martins, C. C. F. Barbosa, L. A. S. de Carvalho, D. S. F. Jorge, F. d. L. Lobo, and E. M. L. d. M. Novo, "Assessment of atmospheric correction methods for Sentinel-2 MSI images applied to Amazon floodplain lakes," *Remote Sens.* **9**, 322 (2017).
38. J. Hedley, A. Harborne, and P. Mumby, "Technical note: Simple and robust removal of sun glint for mapping shallow-water benthos," *Int. J. Remote Sens.* **26**, 2107–2112 (2005).
39. M. Wettle, V. E. Brando, and A. G. Dekker, "A methodology for retrieval of environmental noise equivalent spectra applied to four hyperion scenes of the same tropical coral reef," *Remote Sens. Environ.* **93**, 188–197 (2004).
40. R. A. Garcia, J. D. Hedley, H. C. Tin, and P. R. Fearn, "A method to analyze the potential of optical remote sensing for benthic habitat mapping," *Remote Sens.* **7**, 13157–13189 (2015).
41. K. G. Ruddick, H. J. Gons, M. Rijkeboer, and G. Tilstone, "Optical remote sensing of chlorophyll *a* in case 2 waters by use of an adaptive two-band algorithm with optimal error properties," *Appl. Opt.* **40**, 3575–3585 (2001).
42. S. Bejarano, P. J. Mumby, J. D. Hedley, and I. Sothoran, "Combining optical and acoustic data to enhance the detection of caribbean foreereef habitats," *Remote Sens. Environ.* **114**, 2768–2778 (2010).
43. European Space Agency, "Sentinel-2 captures coral bleaching of Great Barrier Reef, http://www.esa.int/Our_Activities/Observing_the_Earth/Copernicus/Sentinel-2/Sentinel-2_captures_coral_bleaching_of_Great_Barrier_Reef," (2017).
44. A. A. Gitelson, J. F. Schalles, D. C. Rundquist, F. R. Schiebe, and Y. Z. Yacobi, "Comparative reflectance properties of algal cultures with manipulated densities," *J. Appl. Phycol.* **11**, 345–354 (1999).
45. A. Morel and L. Prieur, "Analysis of variations in ocean color," *Limnology and oceanography* **22**, 709–722 (1977).
46. K. Toming, T. Kutser, A. Laas, M. Sepp, B. Paavel, and T. Nõges, "First experiences in mapping lake water quality parameters with Sentinel-2 MSI imagery," *Remote Sens.* **8**, 640 (2016).
47. S. C. Palmer, T. Kutser, and P. D. Hunter, "Remote sensing of inland waters: Challenges, progress and future directions," *Remote Sens. Environ.* **157**, 1–8 (2015).

1. Introduction

Optical remote sensing is of major importance to monitor optically deep and shallow waters from air- and satellite-borne sensors. In the case of optically deep waters, it enables the estimation of the inherent optical properties (IOPs) of the upper water layer, i.e., the spectral absorption and backscattering coefficients. In addition to pure water, the IOPs can be related to three optically active water constituents, namely, phytoplankton, colored dissolved organic matter (CDOM) and non-algal suspended particles. Spatially- and temporally-resolved knowledge of these variables is critical to understand biogeochemical processes such as carbon exchanges, phytoplankton biodiversity shifts, and responses to climatic disturbances [1]. In the case of optically shallow waters, optical remote sensing also enables the estimation of depth and bottom cover (both potentially greatly affecting the water-leaving radiance), which has important implications, e.g., for monitoring coral reefs [2] or detecting seasonal changes in bathymetry [3]. Providing reliable uncertainties (e.g., expressed in terms of mean absolute difference [4] or root mean square deviation [5]) to remote-sensing products is an important task since such knowledge informs one of the confidence level of these products, which is critical for many applications. For example, knowledge of chlorophyll-*a* uncertainty is needed to characterize the uncertainty budget of primary production algorithms [4]. Uncertainties are also required to guide the design of future sensors [6], or to improve the predictions of ocean models through data assimilation [7]. Accurate knowledge of uncertainties is especially critical for remote sensing of aquatic environments, since water absorption often leads to low reflectances compared to other Earth surfaces such as soil or vegetation, and therefore to high uncertainties.

First of all, it is worth reminding that the uncertainty in a given ocean color product has several components, each of which arises from a particular stage of the whole calibration, measurement and processing chain. When assessing uncertainties by comparing the actual product values

measured *in-situ* with their satellite-derived estimates, one actually takes into account the uncertainties related to, e.g., *in-situ* measurements, correction schemes (e.g., atmospheric correction), bio-optical modeling, sensor noise and radiometric specifications, as well as those induced by the inversion method [4,5,8,9]. Note that the uncertainty in the inversion of a particular ocean color parameter usually depends on the actual parameter value itself: for example, in the case of shallow water remote sensing, the uncertainties in the inversion of bathymetry and bottom cover increase with depth since the bottom influence becomes negligible as depth increases. Instead of providing a single uncertainty value for the whole range of possible parameter values, a more informative approach consists in subdividing the parameter space and computing the uncertainty for each subdivision [4, 8, 10]. For example, in [4], the authors characterized the chlorophyll-*a* uncertainty of the Aqua MODerate resolution Imaging Spectroradiometer (MODIS) for eight optical water types, each of which is defined by a mean reflectance spectrum and a spectral covariance matrix. The uncertainty can then be computed for each image pixel based on the memberships to these water types. Still for optically deep waters, other approaches have also been proposed to provide an uncertainty value for each estimate. In [11], the uncertainty is derived from the results of more than 1,000 inversions performed for various spectral shapes of phytoplankton, CDOM and suspended particle IOPs. In [8], it is obtained by propagating uncertainties through the Quasi-Analytical Algorithm. In [1], it is based on the shape of the cost function (that is used for model inversion) around the optimum through the use of the Jacobian matrix.

Simulations have also widely been used to evaluate for some of the uncertainty components. The two main advantages are that (1) one can generate as many simulations as needed, and (2) there is no error in ground truth measurements, correction schemes and modeling, such that only the uncertainties related to the sensor radiometric specifications, the noise model and the inverse method, are evaluated. Such a separation is critical to quantify the influence of each source of uncertainty [5, 6, 8, 9]. The use of simulations is especially interesting for shallow water remote sensing because of the higher number of model parameters compared to deep waters [6]. Simulated data have been used to compare sensors [12] or to identify the main factors confounding the discrimination of coral reefs [6]. However, the number of parameters is such that, for computational convenience, the analysis is often simplified by sampling the parameter space and by using a few bottom covers, sensor configurations or signal-to-noise ratios (SNRs).

Most of the above mentioned approaches thus require remote-sensing data (either real or simulated) to evaluate uncertainties, and the implementation of these approaches may be computationally expensive. In addition, all of them depend on the inversion method, although a wide variety of statistically- and physically-based methods have been developed for remote sensing of optically shallow [13–21] and deep waters [1, 22–24]. Therefore, one cannot know to what extent the uncertainties obtained using a given algorithm could be improved using another one. As emphasized in [6], theoretical studies remain required to characterize the remote-sensing uncertainties, but also to help the design of appropriate sensors.

In this context, the development of Cramer-Rao Bounds (CRBs) is relevant since CRBs provide theoretical lower bounds for the variances of unbiased estimators [25]. For a given water column and noise covariance matrix, the CRB analytical expressions thus directly provide the minimum achievable variances in unbiased estimators for all targeted ocean color geophysical parameters. Since CRBs only depend on the Fisher information related to the modeled reflectance data [25], they are algorithm-independent and do not require one to invert remote-sensing data. Applications of CRBs in remote sensing include polarimetric synthetic aperture radar interferometry [26] or denoising of hyperspectral images [27], but, to our knowledge, they have not been fully developed in the context of ocean color remote sensing. They have only been introduced in [28] for shallow waters in a simple yet not realistic case (i.e., one unknown parameter, known bottom cover, diagonal spectral covariance matrix). However, a more comprehensive study is still required

to evaluate the interest of CRBs for aquatic remote sensing, as knowledge of such minimum inversion uncertainties may be very useful, e.g., to design satellite-borne sensors or to provide lower bounds for remote-sensing data assimilation within oceanic models.

In this paper, we use the reflectance model presented in Section 2 to develop the CRB expressions for both optically deep and shallow waters (Section 3 and Appendix A). Three applications are then presented in Section 4. First, the minimum uncertainties in the inversion of ocean color parameters, as provided by the CRBs, are compared to the experimental estimation standard deviations obtained using the LS (Least-Square) [1, 14] and MILE (Maximum Likelihood estimation including Environmental noise) [21] methods (Section 4.2). Then, the CRBs are used to investigate how perfect *a priori* knowledge on some model parameters can improve the estimation of the remaining unknown parameters (Section 4.3). Finally, the CRBs are used to predict the minimum uncertainties in the inversion of ocean color parameters for four sensor configurations, namely, the HICO (Hyperspectral Imager for the Coastal Ocean), MODIS, Sentinel-2 MSI (MultiSpectral Instrument) and Sentinel-3 OLCI (Ocean and Land Colour Instrument) configurations (Section 4.4). Note that, unless otherwise stated, the term "inversion uncertainty" does not hereafter correspond to the total uncertainty in a given ocean color product. Instead, it refers to the uncertainty in the inversion of a given ocean color parameter, and results from the propagation of uncertainties in the bio-optical modeling of reflectance (such uncertainties being accounted for by the noise model presented in Section 2.1) through the inversion process. The term "inversion uncertainty" is here seen as the estimator standard deviation, provided this estimator is unbiased.

2. Modeling of subsurface remote-sensing reflectance

2.1. Noise probabilistic modeling

Similarly as in [21, 29, 30], the spectral variability of subsurface remote-sensing reflectance $\mathbf{r}_{rs} = [r_{rs}(\lambda_1), \dots, r_{rs}(\lambda_L)]^t$ (where L is the number of wavebands) is described using a multivariate Gaussian distribution, i.e., $\mathbf{r}_{rs} = \boldsymbol{\mu} + \mathbf{n}_s$ where $\boldsymbol{\mu}$ and \mathbf{n}_s are $L \times 1$ vectors. The mean subsurface remote-sensing reflectance spectrum $\boldsymbol{\mu}$ is parameterized using either a shallow (Section 2.2) or deep (Section 2.3) water reflectance model. \mathbf{n}_s is a Gaussian vector with zero mean and covariance matrix $\boldsymbol{\Gamma}_s$ that accounts for the environmental noise [31] (note that all the per-band noise variances are given by the diagonal of $\boldsymbol{\Gamma}_s$). The environmental noise includes all the sources of above-water reflectance variability that are not accounted for by the bio-optical model $\boldsymbol{\mu}$ (e.g., sensor noise, variable residuals from atmospheric correction or effects related to the rough water surface) and may be therefore scene-specific. In practice, it is generally estimated over a homogeneous area of optically deep water.

2.2. Bio-optical modeling for optically shallow waters

For optically shallow waters, the mean subsurface remote-sensing reflectance $\mu(\lambda)$ at a given wavelength λ is given by the semi-analytical model developed in [14, 15, 32]:

$$\mu(\lambda) = r_{rs,\infty}(\lambda) \left\{ 1 - \exp \left[- \left(k_d(\lambda) + k_u^c(\lambda) \right) H \right] \right\} + \frac{1}{\pi} \left[B \rho_{b,1}(\lambda) + (1 - B) \rho_{b,2}(\lambda) \right] \exp \left[- \left(k_d(\lambda) + k_u^b(\lambda) \right) H \right] \quad (1)$$

where $r_{rs,\infty}(\lambda)$ is the deep water reflectance, H is the depth, and the bottom albedo is given by a linear mixture of two substratum albedos $\rho_{b,1}(\lambda)$ and $\rho_{b,2}(\lambda)$ with fractional covers B and $(1 - B)$, respectively. $r_{rs,\infty}(\lambda)$ and the attenuation coefficients $k_d(\lambda)$, $k_u^c(\lambda)$ and $k_u^b(\lambda)$ are further

related to the total absorption ($a(\lambda)$) and backscattering ($b_b(\lambda)$) coefficients [14, 32]:

$$r_{rs,\infty}(\lambda) = \left(0.084 + 0.17 \frac{b_b(\lambda)}{a(\lambda) + b_b(\lambda)} \right) \frac{b_b(\lambda)}{a(\lambda) + b_b(\lambda)} \quad (2)$$

$$k_d(\lambda) = \frac{a(\lambda) + b_b(\lambda)}{\cos \theta_s} \quad (3)$$

$$k_u^c(\lambda) = \frac{1.03}{\cos \theta_v} (a(\lambda) + b_b(\lambda)) \left(1 + 2.4 \frac{b_b(\lambda)}{a(\lambda) + b_b(\lambda)} \right)^{0.5} \quad (4)$$

$$k_u^b(\lambda) = \frac{1.04}{\cos \theta_v} (a(\lambda) + b_b(\lambda)) \left(1 + 5.4 \frac{b_b(\lambda)}{a(\lambda) + b_b(\lambda)} \right)^{0.5} \quad (5)$$

where θ_s and θ_v are respectively the solar and viewing zenith angles. Finally, the absorption and backscattering coefficients are given by the sum of the contributions of optically active water constituents, i.e., pure water, phytoplankton, CDOM and suspended particles [17]:

$$a(\lambda) = a_w(\lambda) + \{a_0(\lambda) + a_1(\lambda) \ln[a_\phi(440)]\} a_\phi(440) + a_g(440) a_g^*(\lambda) \quad (6)$$

$$b_b(\lambda) = b_{bw}(\lambda) + b_{bp}(550) b_{bp}^*(\lambda) \quad (7)$$

where $a_w(\lambda)$ and $b_{bw}(\lambda)$ are the absorption and backscattering coefficients of pure water [33, 34], $a_0(\lambda)$ and $a_1(\lambda)$ are empirical spectra [32], $a_\phi(440)$ is the phytoplankton absorption coefficient at 440 nm, $a_g(440)$ is the CDOM absorption coefficient at 440 nm, $a_g^*(\lambda) = \exp[-0.015(\lambda - 440)]$, $b_{bp}(550)$ is the particle backscattering coefficient at 550 nm and $b_{bp}^*(\lambda) = (550/\lambda)^{0.5}$. Note that, in the following, the known $a_w(\lambda)$, $a_0(\lambda)$, $a_1(\lambda)$, $a_g^*(\lambda)$, $b_{bw}(\lambda)$, $b_{bp}^*(\lambda)$, $\rho_{b,1}(\lambda)$ and $\rho_{b,2}(\lambda)$ spectra were oversampled to 1 nm step before being spectrally-degraded according to each tested sensor radiometric configuration (Section 4.1), assuming a rectangular spectral response for each waveband. For a given sun-sensor geometry, the shallow water reflectance is thus fully determined by the five geophysical parameters H , $a_\phi(440)$, $a_g(440)$, $b_{bp}(550)$ and B .

2.3. Bio-optical modeling for optically deep waters

For optically deep waters, the mean subsurface remote-sensing reflectance is parameterized by

$$\mu(\lambda) = r_{rs,\infty}(\lambda) \quad (8)$$

with $r_{rs,\infty}(\lambda)$ described by Eq. (2), Eq. (6) and Eq. (7). The deep water reflectance is therefore determined by only three geophysical parameters, namely, $a_\phi(440)$, $a_g(440)$, and $b_{bp}(550)$.

3. Development of Cramer-Rao lower bounds

Let us define Δ as the vector of unknown ocean color geophysical parameters (i.e., H , $a_\phi(440)$, $a_g(440)$, $b_{bp}(550)$ and/or B) to be estimated from the remote-sensing observation \mathbf{r}_{rs} (either for optically deep or shallow waters). According to [25], the variance of any unbiased estimator $\hat{\Delta}_i(\mathbf{r}_{rs})$ of any element Δ_i of Δ is bounded as

$$\mathbb{E} \left[(\hat{\Delta}_i(\mathbf{r}_{rs}) - \Delta_i)^2 \right] \geq [\mathbf{CRB}(\Delta)]_{i,i} \quad (9)$$

where $\mathbf{CRB}(\Delta)$ is a square matrix with dimensions equal to the length of Δ . The CRB of Δ_i estimation thus corresponds to the i^{th} element of the diagonal of $\mathbf{CRB}(\Delta)$. Further, the inverse of $\mathbf{CRB}(\Delta)$ is the Fisher information matrix $\mathbf{I}_F(\Delta)$ [25], whose element i, j is

$$[\mathbf{I}_F(\Delta)]_{i,j} = \mathbb{E} \left[\frac{\partial \ln(P(\mathbf{r}_{rs}|\Delta))}{\partial \Delta_i} \frac{\partial \ln(P(\mathbf{r}_{rs}|\Delta))}{\partial \Delta_j} \right] \quad (10)$$

where $P(\mathbf{r}_{r,s}|\mathbf{\Delta})$ is the likelihood of observing $\mathbf{r}_{r,s}$ given $\mathbf{\Delta}$. In the multivariate Gaussian case with mean $\boldsymbol{\mu}$ and covariance matrix $\boldsymbol{\Gamma}_s$ (Section 2.1), Eq. (10) can be simplified [35]:

$$[\mathbf{I}_F(\mathbf{\Delta})]_{i,j} = \frac{1}{2} \text{tr} \left(\boldsymbol{\Gamma}_s^{-1} \frac{\partial \boldsymbol{\Gamma}_s}{\partial \Delta_i} \boldsymbol{\Gamma}_s^{-1} \frac{\partial \boldsymbol{\Gamma}_s}{\partial \Delta_j} \right) + \frac{\partial \boldsymbol{\mu}}{\partial \Delta_i} \boldsymbol{\Gamma}_s^{-1} \frac{\partial \boldsymbol{\mu}}{\partial \Delta_j} \quad (11)$$

where tr is the trace operator. As $\boldsymbol{\Gamma}_s$ does not depend on unknown parameters, Eq. (11) becomes

$$[\mathbf{I}_F(\mathbf{\Delta})]_{i,j} = \frac{\partial \boldsymbol{\mu}}{\partial \Delta_i} \boldsymbol{\Gamma}_s^{-1} \frac{\partial \boldsymbol{\mu}}{\partial \Delta_j}. \quad (12)$$

When using the models described in Section 2, the determination of $\mathbf{I}_F(\mathbf{\Delta})$ thus only requires the calculation of derivatives $\partial \boldsymbol{\mu} / \partial \Delta_i$, as well as the estimation of the environmental noise $\boldsymbol{\Gamma}_s$. The components of $\mathbf{\Delta}$ are H , a_ϕ (440), a_g (440), b_{bp} (550) and/or B in the case of shallow waters (Section 2.2), while they are a_ϕ (440), a_g (440) and/or b_{bp} (550) in the case of deep waters (Section 2.3). The analytical expressions of the five derivatives are developed in Appendix A. $\mathbf{I}_F(\mathbf{\Delta})$ is then inverted numerically using a standard matrix inversion algorithm to obtain the CRB matrix $\mathbf{CRB}(\mathbf{\Delta})$. Based on such a modeling, $\mathbf{CRB}(\mathbf{\Delta})$ only includes the uncertainties related to the considered Fisher information (which depends on the bio-optical model, environmental noise and sensor radiometric specifications), but not those related to, e.g., ground truth measurements, systematic errors in correction schemes (e.g., atmospheric correction), or inverse methods. In other words, $\mathbf{CRB}(\mathbf{\Delta})$ are the minimum uncertainties in $\hat{\Delta}(\mathbf{r}_{r,s})$ due to the propagation of uncertainties in the bio-optical model $\boldsymbol{\mu}$ through the inversion process. Uncertainties in $\boldsymbol{\mu}$ refer to all the factors causing pixel-to-pixel reflectance variations that are not accounted for by $\boldsymbol{\mu}$, such factors being instead described by the noise covariance matrix (in this paper, $\boldsymbol{\Gamma}_s$).

Note that the CRBs provided in Section 4 are actually the square roots of CRBs, denoted $[\mathbf{CRB}(\mathbf{\Delta})]_{i,i}^{0.5}$ for parameter Δ_i (see Eq. (9)). As shown in Eq. (9), $[\mathbf{CRB}(\mathbf{\Delta})]_{i,i}^{0.5}$ has the same nature as a standard deviation and it is thus expressed in the same unit as Δ_i . From a practical point of view, given a set of ocean color parameters $\mathbf{\Delta}$ and a noise covariance matrix $\boldsymbol{\Gamma}_s$, $[\mathbf{CRB}(\mathbf{\Delta})]_{i,i}^{0.5}$ directly provides the minimum estimation standard deviation that can be possibly (but not necessarily) attained by any unbiased estimator $\hat{\Delta}_i(\mathbf{r}_{r,s})$.

4. Experiments and results

4.1. Estimation of environmental noise

A reliable estimate of the environmental noise matrix $\boldsymbol{\Gamma}_s$ based on real data is necessary to obtain consistent CRBs. In this paper, four estimates of $\boldsymbol{\Gamma}_s$ were derived from images acquired by four satellite-borne multi-, super- and hyperspectral sensors, namely Sentinel-2 MSI (MultiSpectral Instrument), HICO (Hyperspectral Imager for the Coastal Ocean), Sentinel-3 OLCI (Ocean and Land Colour Instrument) and MODIS (Table 1).

Table 1. Features of the remote-sensing images used to estimate the environmental noise.

Sensor	Acquisition date	Location	Spatial resolution (m)	Spectral range (nm)	Number of bands
MSI	May 5, 2017	38°45'N, 1°22'E	60	443-783	7
HICO	May 23, 2013	42°50'N, 6°30'E	90	404-799	70
OLCI	July 6, 2017	43°00'N, 10°00'E	300	400-779	13
MODIS	July 17, 2016	41°00'N, 8°00'E	1,000	412-678	10

Besides having different radiometric configurations, these sensors cover a wide range of spatial resolutions, namely, 60 m for MSI (after downsampling the 10 and 20 m bands by averaging over

square cells), 90 m for HICO, 300 m for OLCI full resolution and 1,000 m for MODIS reduced resolution. While the spatial resolutions and the radiometric configurations of MODIS and OLCI have been designed to monitor oceanic and coastal waters from regional to global scales, the high spatial resolution provided by MSI is convenient to monitor coastal and inland waters from local to regional scales. Incidentally, note that the inversion performances obtained using the original 10 m and/or 20 m resolution MSI bands (which are obviously noisier than the 60 m resolution bands used in this paper) cannot be better than the CRBs of MSI shown in Section 4.4. Finally, though being no longer operational, HICO was also included in this study because it provided both high spatial and spectral resolutions as well as a high SNR, all of which are critical to study shallow areas.

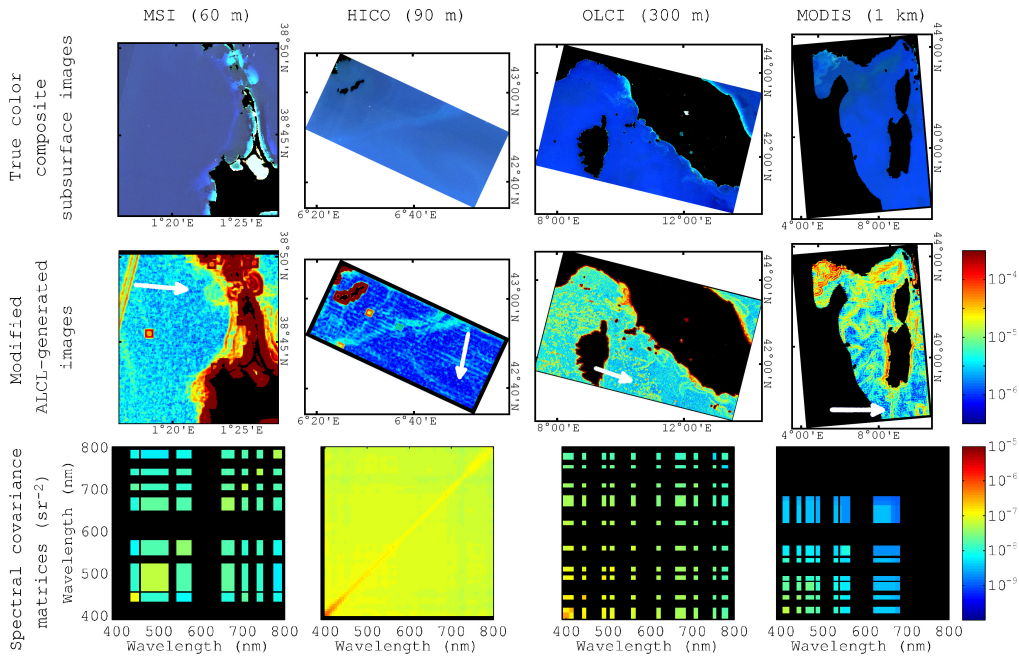


Fig. 1. Environmental noise estimation based on the MSI, HICO, OLCI and MODIS (columns 1 to 4, resp.) images (row 1), where unreliable pixels (e.g., land and clouds) are masked. For each image, the white arrow in row 2 indicates the minimum of the modified ALCL-generated image (corresponding to the most homogeneous area), where the Γ_s matrix (row 3) is estimated. In row 3, the size of each uniformly colored area denotes the sensor bandwidths at the corresponding wavebands (no spectral data measured in the black areas). Note that the colorbar is the same for each row.

The satellite images used for Γ_s estimation were acquired over the Western Mediterranean region. They were directly obtained at Level-2A (Fig. 1). The MSI bottom-of-atmosphere reflectance image (dimensionless) was downloaded from the Copernicus Open Access Hub (scihub.copernicus.eu/dhus/#/home) and converted into remote-sensing reflectance by dividing it by a factor of π . Note that, although the Sentinel-2 Sen2cor toolbox used for atmospheric correction was not originally designed for aquatic scenes, several recent studies showed that it could allow satisfactory estimations of water reflectance [36, 37]. The HICO remote-sensing reflectance image was provided by the Oregon State University, College of Earth, Ocean, and Atmospheric Sciences (hico.coas.oregonstate.edu). The OLCI marine product (dimensionless) was downloaded from the Copernicus Online Data Access (coda.eumetsat.int) and converted into remote-sensing reflectance by dividing it by a

factor of π . Finally, the MODIS remote-sensing reflectance image was obtained from the NASA Ocean Color data archive (oceancolor.gsfc.nasa.gov).

While sunglint was found to have a negligible influence on the considered OLCI and MODIS coarse spatial resolution data (especially due to the tilted viewing configuration of OLCI), it was corrected for MSI and HICO data by using the algorithm proposed in [38]. For this purpose, note that, for both MSI and HICO sensors, the near-infrared reflectance used in the deglint algorithm was the band value at 842 nm for MSI, and the value averaged over the ten bands located between 800 and 850 nm for HICO. Estimating the sunglint contribution outside the spectral range where Γ_s was derived, ensures that the environmental noise is not underestimated at all the considered wavebands (because the sunglint contribution is basically subtracted from all these wavebands). Finally, subsurface remote-sensing reflectance data were obtained after correcting for the air/water interface [23].

For each image, the Automated Local Convergence Locator (ALCL) method [39] was implemented to find a homogeneous area of optically-deep water in the image, where Γ_s could then be objectively and reliably estimated (Fig. 1). ALCL consists in finding an area where the spectrally-averaged standard deviation of reflectance computed over a square cell does not change when increasing the cell size. The ALCL criterion to be minimized is the slope of the linear regression between the reflectance standard deviation and the cell size. In this paper, the ALCL criterion was multiplied by the spectrally-averaged standard deviation of reflectance at the maximum cell size in order to favor areas of low environmental noise. As shown in Fig. 1, such a modified ALCL criterion takes higher values around coastal areas, where the water column may be highly spatially variable. Note also the red squares on the modified ALCL-generated maps of MSI and HICO that indicate the presence of boats and boat-induced waves (Fig. 1). On the other hand, the modified ALCL criterion takes lower values over homogeneous deep water areas (Fig. 1). Implementing an ALCL-like algorithm is critical as it ensures that, in the selected area, the spectral variability is only due to the environmental noise and not to possible changes in bathymetry, bottom type and/or water clarity.

The HICO configuration is used in Section 4.2, Section 4.3 and Section 4.4, because, as a hyperspectral sensor, HICO can accurately characterize both deep and shallow waters due to its large number of narrow wavebands. The other sensor configurations are used in Section 4.4.

4.2. Using CRBs to assess the performances of ocean color remote-sensing methods

4.2.1. Ocean color remote-sensing methods

In this study, the minimum inversion uncertainties provided by CRBs are compared to the experimental estimation uncertainties obtained using two published methods [1, 14, 21]. Both methods consist in iteratively optimizing a cost function that relates the measured reflectance \mathbf{r}_{rs} and the model $\boldsymbol{\mu} = \boldsymbol{\mu}(\boldsymbol{\Delta})$ (Eq. (1) and Eq. (8)) in order to derive the ocean color geophysical parameters $\boldsymbol{\Delta}$. The widely used Least-Square (LS) estimator [1, 14] is given by

$$\hat{\boldsymbol{\Delta}}_{LS}(\mathbf{r}_{rs}) = \underset{\boldsymbol{\Delta}}{\operatorname{argmin}} [(\mathbf{r}_{rs} - \boldsymbol{\mu}(\boldsymbol{\Delta}))^t (\mathbf{r}_{rs} - \boldsymbol{\mu}(\boldsymbol{\Delta}))]. \quad (13)$$

The MILE (Maximum Likelihood estimation including Environmental noise) estimator [21] utilizes the covariance matrix $\boldsymbol{\Gamma}_s$ and is given by the minimum of the Mahalanobis distance:

$$\hat{\boldsymbol{\Delta}}_{MILE}(\mathbf{r}_{rs}) = \underset{\boldsymbol{\Delta}}{\operatorname{argmin}} [(\mathbf{r}_{rs} - \boldsymbol{\mu}(\boldsymbol{\Delta}))^t \boldsymbol{\Gamma}_s^{-1} (\mathbf{r}_{rs} - \boldsymbol{\mu}(\boldsymbol{\Delta}))]. \quad (14)$$

4.2.2. Optically shallow waters

LS and MILE are compared based on a synthetic hyperspectral data set generated similarly as in [21, 29, 30]. The wavebands considered here were those of HICO, as introduced in Section 4.1. The water column influence was studied for various depth values, ranging from 0.5 to 15 m by 1 m

step. All the remaining model parameters were fixed. In particular, we considered an intermediate water clarity [40], i.e., $a_\phi(440) = 0.05 \text{ m}^{-1}$, $a_g(440) = 0.1 \text{ m}^{-1}$, and $b_{bp}(550) = 0.01 \text{ m}^{-1}$. The bottom was defined as a linear mixture of 50% sand and 50% seagrasses, both reflectance spectra being extracted from the data set presented in [21]. Finally, the solar and viewing zenith angles were set to 35° and 0° , respectively. For each depth value, the “mvnrnd” MATLAB function was used to randomly generate 2,000 noise-perturbed spectra using the model in Eq. (1) as the mean vector and the HICO Γ_s matrix (Fig. 1) as the spectral covariance matrix. Each spectrum was then inverted using LS and MILE to estimate the unknown vector of parameters $\Delta = [H, a_\phi(440), a_g(440), b_{bp}(550), B]$. Note that initialization was performed using a Latin Hypercube Sampling scheme as detailed in [21]. For each depth value and each parameter Δ_i , the experimental standard deviations of LS and MILE estimates (hereafter referred to as LS and MILE inversion uncertainties) were calculated over the 2,000 samples and compared to $[\text{CRB}(\Delta)]_{i,i}^{0.5}$ (Eq. (9)). Note that the optimization domain was not bounded since setting lower and upper bounds amounts to introducing *a priori* knowledge within the inversion, which may make the comparison with CRBs misleading when the inversion uncertainty is high. Preliminary tests actually showed that bounding the optimization domain had a negligible effect on the retrieval, the only non-negligible influence being observed for H and B estimations over quasi optically deep waters. The experimental estimation biases (i.e., estimates of systematic errors) are not presented here as they were found to be mostly negligible for every parameter and both methods when H is lower than 10-15 m. Note that, for higher depths, compensations between H and B may lead to non-negligible biases (that increase with H) for both parameters [21], thus implying that the inversion uncertainty cannot be represented only by CRBs but also by biases.

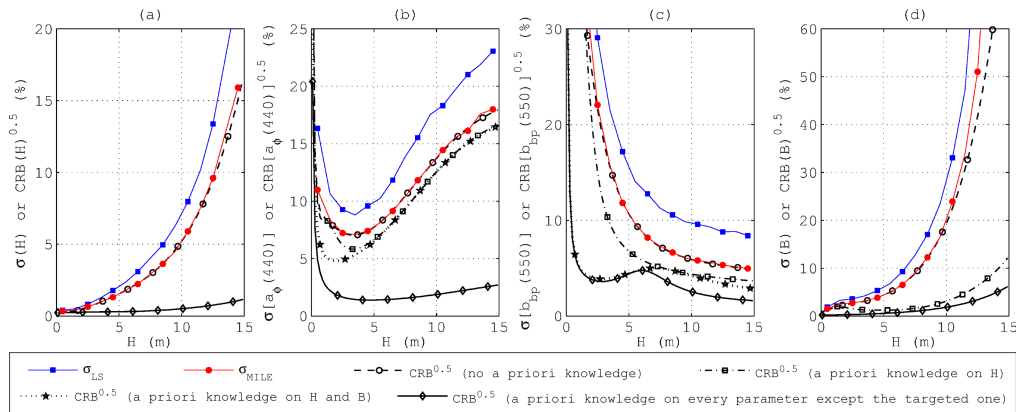


Fig. 2. Square roots of CRBs of (a) H , (b) $a_\phi(440)$, (c) $b_{bp}(550)$ and (d) B (all in [%]) versus depth for optically shallow water and HICO configuration. Other model parameters are fixed: $a_\phi(440) = 0.05 \text{ m}^{-1}$, $a_g(440) = 0.1 \text{ m}^{-1}$, $b_{bp}(550) = 0.01 \text{ m}^{-1}$, and the bottom is a mix of sand and seagrasses with $B = 0.5$. Various situations are considered: no *a priori* knowledge (Section 4.2.2), and perfect *a priori* knowledge on H , on both H and B , or on every parameter except the targeted one (Section 4.3.1). The LS and MILE experimental standard deviations obtained without *a priori* knowledge are also displayed.

The results show that the CRBs obtained without *a priori* knowledge vary similarly to LS and MILE inversion uncertainties (Fig. 2). For example, due to the decreasing bottom detectability, the CRBs of H and B increase with depth and reach 17 and 85%, respectively, for $H = 15$ m. Also, the estimation of water clarity parameters (i.e., $a_\phi(440)$ and $b_{bp}(550)$ in Fig. 2) becomes unreliable for very shallow waters as the bottom influence on water-leaving radiance overshadows those of water constituents [12, 20]. Note that this would be even more critical if the bottom intra-class variability (which is one of the most confounding factors for shallow water remote

sensing [29]) could be taken into account in the modeling. The decrease in performance observed for such shallow waters is markedly more visible for $b_{bp}(550)$ estimation (whose CRB reaches 60% for $H = 0.50$ m) because the spectral signatures of sand and particle backscattering are similar, i.e., both increase the reflectance at all wavebands.

The results also show that the MILE inversion uncertainties almost equal the CRBs for every parameter and $H \leq 10$ m, i.e., the MILE estimator is efficient [25]. This result theoretically demonstrates that no method can perform significantly better than MILE if the bio-optical and probabilistic models are perfect. Note that such a conclusion may change when using actual spectra for which the water column may be not accurately described by the models. For $H \geq 10$ m, progressively increasing biases may lead LS and MILE inversion uncertainties for H and B to increase with depth faster than the CRBs.

4.2.3. Optically deep waters

LS and MILE are also compared based on a synthetic HICO-like hyperspectral data set corresponding to optically deep waters. Unlike optically shallow waters for which depth and bottom cover can vary independently from water clarity, optically deep waters generally show correlations between phytoplankton, CDOM and suspended particle concentrations (especially in the open ocean). In this paper, these correlations are taken into account by assessing LS and MILE inversion uncertainties for the eight water optical types defined in [4]. For each type, the mean subsurface remote-sensing reflectance spectrum provided in [4] was inverted using LS and the model in Eq. (8). This resulted in eight sets of $a_\phi(440)$, $a_g(440)$ and $b_{bp}(550)$ values corresponding to an increasing turbidity, ranging from low-chlorophyll blue waters to turbid sediment-dominated waters (Table 2). For each of these eight sets, the same methodology as for shallow waters was then applied to generate 2,000 noise-perturbed spectra based on the HICO \mathbf{I}_s matrix, to invert the model (Eq. (8)) and to compute the experimental standard deviations of $a_\phi(440)$, $a_g(440)$ and $b_{bp}(550)$ estimates. Note that the experimental estimation bias was negligible (i.e., well below 10%) for the three parameters and the two methods, thus making CRBs appropriate indicators of minimum achievable inversion uncertainties.

Overall, for every water type, the CRBs obtained without *a priori* knowledge vary similarly to LS and MILE inversion uncertainties (Fig. 3). In the case of absorbing components (Figs. 3(a) and 3(b)), the CRBs of $a_\phi(440)$ and $a_g(440)$ depend on the $a_g(440)/a_\phi(440)$ ratio as noticed in [10]. For example, for types 1 to 3, the total water absorption in the blue-green domain is dominated by CDOM for these simulations (Table 2), meaning that the CDOM influence overshadows that of phytoplankton [10]. $a_g(440)$ (whose CRB ranges between 6 and 13%) can therefore be estimated more accurately than $a_\phi(440)$ (whose CRB ranges between 16 and 30%). Also, the retrieval accuracies of $a_\phi(440)$ and $a_g(440)$ increase with backscattering (see types 5 to 8 in Figs. 3(a) and 3(b)). As also demonstrated, e.g., in [41], higher backscattering indeed leads to higher reflectance, and therefore, to higher SNR and improved estimation accuracies.

Particle backscattering (whose CRB is lower than 7% for every water type) can generally be retrieved more accurately than $a_\phi(440)$ and $a_g(440)$ (Fig. 3(c)), which is in agreement with previous findings [10, 11]. For a given value of $b_{bp}(550)$, the CRB of $b_{bp}(550)$ increases with total absorption (see types 1 to 3 in Fig. 3(c)) due to the corresponding decreases in reflectance and SNR. On the contrary, $b_{bp}(550)$ can be estimated more accurately for higher $b_{bp}(550)$ values for the same reasons as for $a_\phi(440)$ and $a_g(440)$, i.e., due to the increase in SNR (see types 5 to 8 in Fig. 3(c)).

Similarly to shallow waters, for the three parameters, the MILE inversion uncertainties are closer to the CRBs than are the LS ones, demonstrating the interest of taking spectral covariance into account when inverting the model based on HICO data [24]. Note that this is more evident for $b_{bp}(550)$ estimation as also observed in [24]. This may be due to the fact that the water-leaving radiance is affected more similarly over all wavebands by particle backscattering

Table 2. $a_\phi(440)$, $a_g(440)$ and $b_{bp}(550)$ estimated values for the water types defined in [4].

Water type	$a_\phi(440)$ (m^{-1})	$a_g(440)$ (m^{-1})	$b_{bp}(550)$ (m^{-1})
1	0.002	0.008	0.002
2	0.006	0.013	0.002
3	0.015	0.020	0.002
4	0.039	0.038	0.003
5	0.094	0.081	0.004
6	0.149	0.144	0.019
7	0.136	0.103	0.029
8	0.116	0.142	0.052

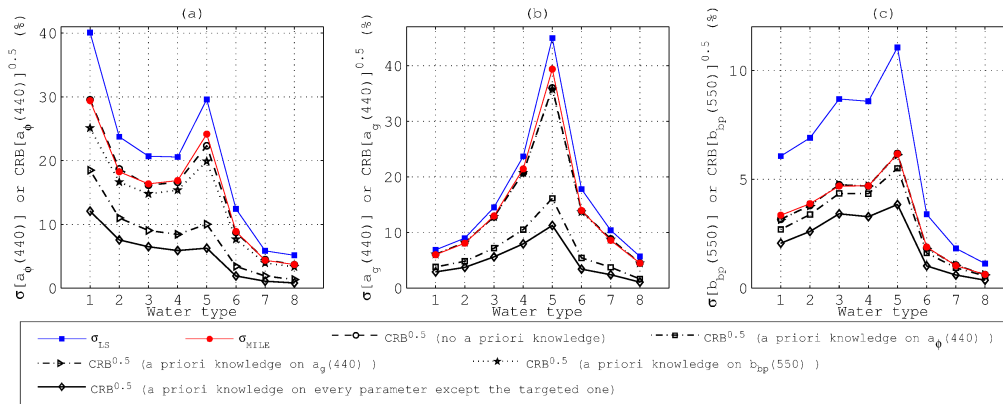


Fig. 3. Square roots of CRBs of (a) $a_\phi(440)$, (b) $a_g(440)$ and (c) $b_{bp}(550)$ (all in [%]) for optically deep water and HICO configuration, and for the eight water types defined in [4] and corresponding to the parameter values shown in Table 2. Various situations are considered: no *a priori* knowledge (Section 4.2.3), and perfect *a priori* knowledge on $a_\phi(440)$, on $a_g(440)$, on $b_{bp}(550)$, or on every parameter except the targeted one (Section 4.3.2). The LS and MILE experimental standard deviations obtained without a *a priori* knowledge are also displayed.

than by phytoplankton and CDOM absorptions (due to locally strong absorption features).

The results obtained without *a priori* knowledge for both optically shallow (Fig. 2) and deep waters (Fig. 3) show that, overall, the CRBs accurately describe the experimental estimation standard deviations obtained from simulated reflectance data. Therefore, no simulations and inversions will be performed in the following when investigating the influence of perfect *a priori* knowledge on model inversion (Section 4.3) and when presenting the CRBs obtained for MSI, OLCI and MODIS configurations (Section 4.4).

4.3. Using CRBs to assess the influence of *a priori* knowledge on model inversion

CRBs can be used to study how perfect *a priori* knowledge on some of the ocean color parameter(s) improves the estimation of remaining unknown parameters [26]. For example, for shallow waters, depth may be known from a LiDAR- or acoustic-derived bathymetric map, and used as an input to the inversion algorithm. In the latter case, $\Delta = [a_\phi(440), a_g(440), b_{bp}(550), B]$, so $I_F(\Delta)$ and $CRB(\Delta)$ become 4×4 matrices. Note that such a study can also provide useful information on the interest of strictly bounding the optimization domain for one or several parameter(s) during model inversion (if the water column is sufficiently well known *a priori*), so as to significantly improve the estimation of remaining parameters.

4.3.1. Optically shallow waters

Figure 2(b) shows that, for the considered simulation conditions, using perfect *a priori* knowledge on H has little effect on $a_\phi(440)$ retrieval. It has slightly more influence on $b_{bp}(550)$ estimation, e.g., at 5 m, the CRB is about two-fold lower than that obtained without *a priori* knowledge (Fig. 2(c)). However, the greatest gain in performance is obtained for B retrieval (Fig. 2(d)), whose CRB is seven-fold lower at 15 m when using perfect *a priori* knowledge on H . Such knowledge indeed prevents the compensations between H and B as mentioned in Section 4.2.2. Combining optical data with acoustic or LiDAR data thus appears to be relevant to improve the remote sensing of benthic habitats, confirming the results obtained in [42] based on real data.

Using perfect *a priori* knowledge on both H and B significantly improves the $a_\phi(440)$ retrieval for very shallow waters only (e.g., by a factor 1.6 for $H = 1$ m), for which the bottom has the strongest influence (Fig. 2(b)). It has a much stronger influence on $b_{bp}(550)$ estimation, whose CRB at 1 m depth is seven-fold lower than that obtained without *a priori* knowledge (Fig. 2(c)). This improvement is mainly due to the similar spectral signatures of sandy bottoms and particle backscattering (Section 4.2.2): knowing the former significantly enhances the retrieval of the latter. Interestingly, this result theoretically proves the relevance of the Shallow Water Inversion Model [19] that uses known benthic albedo and bathymetric maps as inputs to the inversion algorithm to improve the remote sensing of water composition in shallow waters.

Ultimately, as expected, the highest increase in performance is obtained when all the parameters except the one to be estimated are known.

4.3.2. Optically deep waters

Figures 3(a) and 3(b) show that, for the eight water types, the CRB of $a_\phi(440)$ (resp., $a_g(440)$) is about two-fold lower when $a_g(440)$ (resp., $a_\phi(440)$) is known, and is close to the CRB obtained with known $a_g(440)$ and $b_{bp}(550)$ (resp., $a_\phi(440)$ and $b_{bp}(550)$). In other words, the accuracy of $a_\phi(440)$ retrieval mainly depends on that of $a_g(440)$ retrieval and reciprocally. In particular, such a result indicates that the use of long ultraviolet bands (characterized by low chlorophyll absorption and high CDOM absorption) as suggested in [1] should be helpful in improving the decoupling and retrieval of both absorbing components. Figures 3(b) and 3(c) also show that the $a_g(440)$ and $b_{bp}(550)$ retrievals are uncorrelated, since knowledge on $b_{bp}(550)$ does not improve $a_g(440)$ estimation and reciprocally. CDOM absorption indeed affects the water-leaving radiance mainly in the blue-green domain while particle backscattering affects the radiance at all wavebands, which allows both effects to be accurately identified.

4.4. Using CRBs to predict minimum inversion uncertainties for MSI, HICO, OLCI and MODIS radiometric configurations

Beforehand, it is worth emphasizing that the CRBs of the four investigated sensors depend on various factors, including not only their radiometric configurations (e.g., number and position of wavebands, as well as their bandwidths) but also their spatial resolutions for example. Therefore, the effects of these factors on CRBs cannot be distinguished from each other based on the following results only. Furthermore, the environmental noise covariance matrices presented in Fig. 1 may be scene-specific, leading in turn to somewhat scene-specific CRBs as well. These important aspects must be kept in mind in the following when comparing the CRBs.

4.4.1. Optically shallow waters

In Fig. 4, CRBs are represented for the same depth range, water composition and bottom cover as in Fig. 2. Overall, MODIS obtains lower CRBs than the other sensors for H , $a_\phi(440)$, $b_{bp}(550)$ and B . While this result indicates that MODIS can theoretically remotely sense shallow waters with a satisfactory accuracy, the low spatial resolution considered here (1 km) generally makes this sensor inappropriate for such applications due to the difficulty in properly focusing on coastal

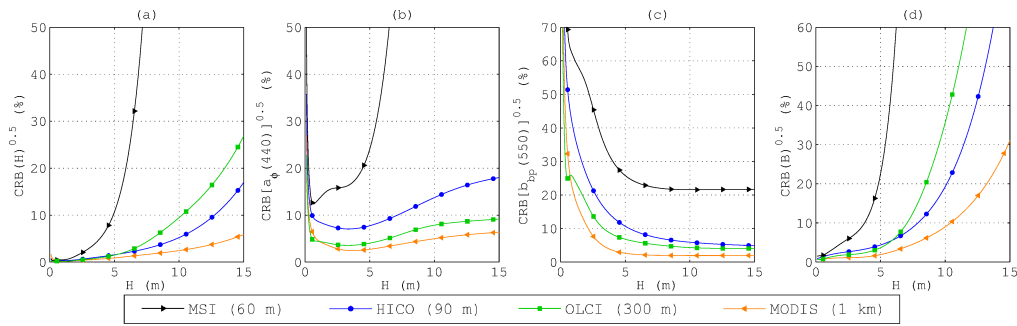


Fig. 4. Square roots of CRBs of (a) H , (b) $a_{\phi}(440)$, (c) $b_{bp}(550)$ and (d) B (all in [%]) versus depth for optically shallow water and MSI, HICO, OLCI and MODIS configurations. Other model parameters are fixed: $a_{\phi}(440) = 0.05 \text{ m}^{-1}$, $a_g(440) = 0.1 \text{ m}^{-1}$, $b_{bp}(550) = 0.01 \text{ m}^{-1}$, and the bottom is a mix of sand and seagrasses with $B = 0.5$.

areas. Similar conclusions can be drawn about the CRBs of OLCI, although its higher spatial resolution (300 m) may allow OLCI to characterize some large coastal areas.

Actually, only the spatial resolutions of HICO (90 m) and MSI (60 m) are adapted for shallow water remote sensing. As a hyperspectral sensor, which has been shown to better identify the influences of all parameters than multispectral sensors [10, 12], and despite its generally higher noise variances per band for the considered scenes (Fig. 1), HICO provides significantly lower CRBs than MSI (bearing in mind that HICO has a coarser spatial resolution). Such a result emphasizes the great potential of HICO-like sensors for accurately characterizing coastal areas.

Though not being specifically developed for shallow water remote sensing, MSI provides accurate inversion performances for H , B and, to a lesser extent, $a_{\phi}(440)$, for $H \leq 5 \text{ m}$ with CRBs generally lower than 25%. The high spatial and temporal resolutions offered by Sentinel-2 MSI thus make it an outstanding opportunity to monitor environments such as shallow coral reefs (e.g., to detect coral bleaching) that are an important subject of on-going research within the Sen2Coral ESA project, e.g., [43]. Except for $b_{bp}(550)$, MSI generally shows high CRBs when $H > 5 \text{ m}$. In this case, water absorption is such that the bottom is nearly invisible at the four wavebands beyond 650 nm (see the MSI wavebands in Fig. 1). For $H > 5 \text{ m}$ and the considered water and substrate compositions, the influences of all the parameters except $b_{bp}(550)$ can be mainly observed in the first three remaining wavebands. This means that, without *a priori* knowledge on H , $a_{\phi}(440)$, $a_g(440)$ and/or B , the inversion is ill-posed and thus leads to poor estimation results for these four parameters. Meanwhile, $b_{bp}(550)$ can still be accurately retrieved because it also affects the reflectance at the last four wavebands. Beyond a given limiting optical depth, further constraining the inversion (e.g., by setting strict lower and upper bounds for some of the parameters to be retrieved) is thus required to improve the overall retrieval (note that the relevance of strictly bounding each parameter can be investigated as proposed in Section 4.3). It is worth emphasizing that such a limiting optical depth (and more generally, all the CRBs shown in Fig. 2 and Fig. 4) not only depends on depth, but also on water and substrate compositions. For example, the CRB of H could be shown to decrease when the water clarity and substrate brightness increase.

4.4.2. Optically deep waters

In Fig. 5 and Fig. 6, the CRBs of $a_{\phi}(440)$ and $b_{bp}(550)$ are plotted for a wide variety of oceanic, coastal and inland waters. Note that this representation does not consider correlations between parameters, so some of the presented $a_{\phi}(440)$ and $b_{bp}(550)$ combinations are unlikely to occur in natural waters, e.g., high $a_{\phi}(440)$ and low $b_{bp}(550)$ [44]. Yet, Fig. 5 and Fig. 6 provide a more comprehensive overview of the waters possibly encountered on Earth than the water types

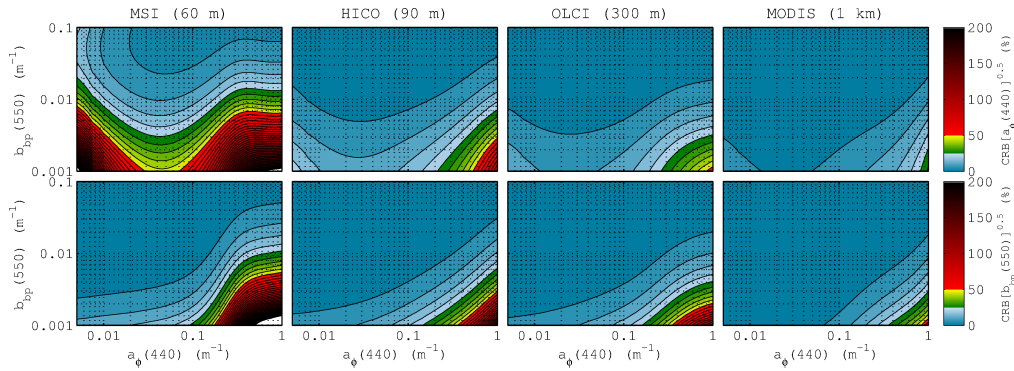


Fig. 5. Square roots of CRBs of $a_\phi(440)$ (row 1) and $b_{bp}(550)$ (row 2) (all in [%]) versus $a_\phi(440)$ and $b_{bp}(550)$ for optically deep water and MSI, HICO, OLCI and MODIS (columns 1 to 4, resp.) configurations. $a_g(440)$ is set to 0.01 m^{-1} . Isolines are represented every 5%. White areas correspond to CRB values higher than 200%.

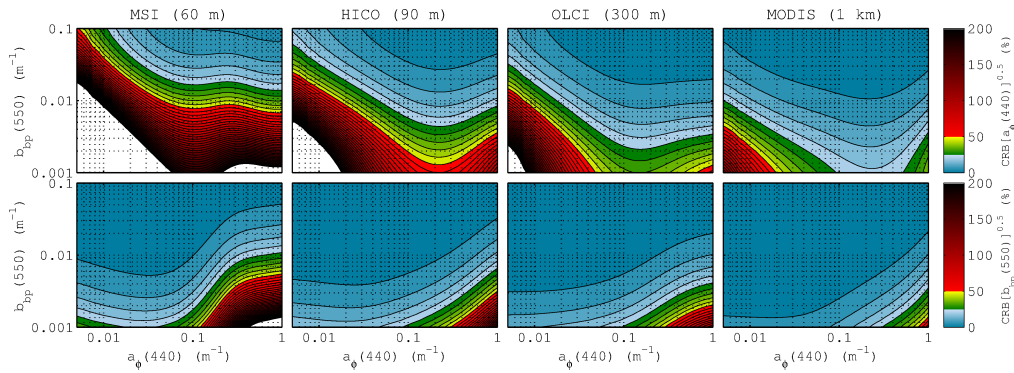


Fig. 6. Same as Fig. 5, but with $a_g(440) = 0.12 \text{ m}^{-1}$.

defined in [4]. Note that the ranges of CRB values obtained for Case-1 clear oceanic and Case-2 coastal and inland deep waters [45] (Fig. 5, Fig. 6) are further emphasized in Table 3.

The CRBs of $a_\phi(440)$ and $b_{bp}(550)$ show similar patterns for the four sensors. For a given $b_{bp}(550)$ value, the CRB of $a_\phi(440)$ (row 1 in Fig. 5 and Fig. 6) generally shows a bowl-shaped pattern with respect to $a_\phi(440)$. It is minimum at the value $a_{\phi,min}(440)$, with $a_{\phi,min}(440)$ slightly greater than $a_g(440)$ ($a_{\phi,min}(440) \approx 0.03 \text{ m}^{-1}$ for Fig. 5 and $a_{\phi,min}(440) \approx 0.15 \text{ m}^{-1}$ for Fig. 6). For $a_\phi(440) < a_{\phi,min}(440)$, the CRB of $a_\phi(440)$ increases due to the overshadowing influence of CDOM (Section 4.2.3), while for $a_\phi(440) > a_{\phi,min}(440)$, the increase is due to the decreasing SNR and progressive reflectance saturation. For a given $b_{bp}(550)$ value, the CRB of $b_{bp}(550)$ generally increases with $a_\phi(440)$ and is less dependent on $a_g(440)$ than the CRB of $a_\phi(440)$ (row 2 in Fig. 5 and Fig. 6). Finally, for a given $a_\phi(440)$ value, the CRBs of $a_\phi(440)$ and $b_{bp}(550)$ decrease as $b_{bp}(550)$ increases due to the associated increase in SNR (Section 4.2.3).

Because of the convenient choice of wavebands as well as its coarser spatial resolution leading to higher SNRs as compared to the other tested sensors (Fig. 1), MODIS mostly obtains the best CRBs for $a_\phi(440)$ and $b_{bp}(550)$, i.e., generally below 25%, for the two $a_g(440)$ values (Fig. 5 and Fig. 6). For Case-1 waters, the CRBs are even lower than 8% (Fig. 5 and Table 3), thus demonstrating the strong potential of MODIS for mapping water clarity at the global scale.

Overall, for both $a_g(440)$ values, the CRBs of HICO and OLCI show rather similar patterns.

Table 3. Ranges of square roots of $a_\phi(440)$ and $b_{bp}(550)$ CRBs (all in [%]) observed in Fig. 5 and Fig. 6 for Case-1 ($0.005 \leq a_\phi(440) \leq 0.03 \text{ m}^{-1}$, $a_g(440) = 0.01 \text{ m}^{-1}$, $0.001 \leq b_{bp}(550) \leq 0.003 \text{ m}^{-1}$) and Case-2 ($0.1 \leq a_\phi(440) \leq 1 \text{ m}^{-1}$, $a_g(440) = 0.12 \text{ m}^{-1}$, $0.01 \leq b_{bp}(550) \leq 0.1 \text{ m}^{-1}$) deep waters and MSI, HICO, OLCI and MODIS configurations.

	Case-1 clear oceanic waters		Case-2 coastal and inland waters	
	$a_\phi(440)$	$b_{bp}(550)$	$a_\phi(440)$	$b_{bp}(550)$
MSI (60 m)	27 - 216	4 - 16	3 - 45	1 - 27
HICO (90 m)	7 - 23	2 - 11	1 - 22	0 - 17
OLCI (300 m)	5 - 15	2 - 10	1 - 10	0 - 10
MODIS (1 km)	2 - 8	1 - 3	1 - 12	0 - 10

For Case-1 waters, the CRBs obtained for these two sensors range between 5 and 23% for $a_\phi(440)$, and between 2 and 11% for $b_{bp}(550)$ (Fig. 5 and Table 3). Their higher spatial resolutions as compared to MODIS also allows them to conveniently monitor Case-2 coastal and inland waters. For such waters, the CRBs of HICO and OLCI are, respectively, better than 22 and 10% for $a_\phi(440)$, while they are, respectively, better than 17 and 10% for $b_{bp}(550)$ (Fig. 6 and Table 3). These results thus emphasize the potential of these two sensors for characterizing a wide range of waters, ranging from oceanic clear waters to coastal and inland turbid waters. The comparable CRBs obtained for OLCI and HICO also suggest that a lower SNR (e.g., due to a finer spatial resolution) may be somewhat compensated for by a higher number of bands (potentially leading to a higher amount of information).

Overall, MSI provides higher CRBs compared to HICO, OLCI and MODIS. For example, the CRB of $a_\phi(440)$ cannot be better than 27% for Case-1 waters, and even dramatically increases up to more than 200% for very low values of $a_\phi(440)$ and $b_{bp}(550)$ (Fig. 5 and Table 3). These poorer performances are not only due to the finer spatial resolution of MSI (that limits the SNR), but also to its lower number of bands and coarser spectral resolution in the chlorophyll-sensitive 400-700 nm domain (Fig. 1). However, MSI enables a more accurate $a_\phi(440)$ retrieval over Case-2 waters, the associated CRB ranging from 3 to 45% (Fig. 6 and Table 3). For such turbid waters, the red-edge MSI band at 705 nm is critical to achieve these performances as it enables the amplitude of the reflectance peak near 700 nm (that correlates with phytoplankton concentration [44]) to be captured. Note that the good performances obtained for Case-2 waters are in agreement with the recent results obtained in [46] using actual MSI data. Finally, it is worth noting that the MSI CRB for $b_{bp}(550)$ is better than 27% for both Case-1 and Case-2 waters (Fig. 5, Fig. 6 and Table 3). These results thus suggest that MSI could be used for detecting and tracking sediment plumes and algal blooms at fine spatial and temporal scales. This is especially important for monitoring coastal and inland waters that have a smaller geographic footprint compared to the open ocean [47].

5. Conclusions and perspectives

This study focuses on the development and application of Cramer-Rao bounds (CRBs) for ocean color remote sensing of deep and shallow waters. In both cases, the CRBs are computed using standard probabilistic and bio-optical models that represent the variability of water subsurface remote-sensing reflectance. Overall, CRBs are shown to provide valuable information about the best inversion performances that may be expected for a given sensor configuration and a given application. In this paper, CRBs are used to evaluate the efficiency of the LS and MILE inversion methods and to investigate to what extent the use of perfect *a priori* knowledge on one or several ocean color geophysical parameters can improve the estimation of remaining unknown parameters. In addition, CRBs are used to predict the minimum uncertainties in the inversion of ocean color

geophysical parameters for four sensor configurations, namely Sentinel-2 MSI, HICO, Sentinel-3 OLCI and MODIS. For example, for the above-defined Case-1 deep waters, the CRBs of OLCI range from 5 to 15% for $a_\phi(440)$, and from 2 to 10% for $b_{bp}(550)$. Also, for the above-defined Case-2 deep waters, the CRBs of MSI range from 3 to 45% for $a_\phi(440)$, and from 1 to 27% for $b_{bp}(550)$. As demonstrated in this paper, CRBs vary with the values of ocean color geophysical parameters in a very complex way for both deep and shallow waters. Since CRBs are based on analytical expressions and do not require one to invert remote-sensing reflectance data, they can be efficiently calculated for any set of parameters. Importantly, the proposed CRBs only depend on the considered Fisher information related to the models presented in Section 2. Therefore, uncertainties due to, e.g., ground truth measurements, inversion algorithm or systematic errors in atmospheric correction and reflectance modeling, must be added when evaluating the total uncertainty budget for a given ocean color geophysical product. Such additional uncertainties explain the differences observed between the $a_\phi(440)$ CRBs of MODIS (Fig. 5 and Fig. 6) and the chlorophyll-*a* uncertainties presented in [4].

Many perspectives emerge from this study. CRBs have been demonstrated to be useful to explore the potential of multi- and hyperspectral sensors for a given application (e.g., coral reef remote sensing in shallow waters). Therefore, CRBs could not only be calculated for other operational sensors, but also serve as a convenient basis to design forthcoming ones. For example, deriving CRBs using environmental noise matrices estimated from different spectrally-degraded versions of the same HICO image could allow one to compare sensors for the same amount of measured photons and, therefore, to focus on the influence of the radiometric configuration (number and position of wavebands, bandwidths). Alternatively, one could use CRBs to predict the gain in estimation performance expected when degrading the spatial resolution of a given satellite image (thus improving the SNR), if this resolution is not a limiting factor. Another interesting prospect would be to assess the variability of CRBs when the environmental noise changes across different scenes acquired with the same sensor. Perspectives also include (1) determining CRBs for other bio-optical or noise models (e.g., deriving CRBs from the MILEBI noise model [21] could allow one to include uncertainties in bio-optically modeled shallow water reflectance that are not only due to the environmental noise but also to the bottom intra-class variability), (2) integrating possible *a priori* information on parameter distributions (e.g., as given by lower and upper bounds) into classical CRBs through the use of Bayesian CRBs, (3) studying the influence of sun-sensor geometry on the inversion, or (4) investigating the capability of remote sensing in differentiating various phytoplankton species or in discriminating various bottom covers.

Appendix A: development of $\partial\mu/\partial\Delta_i$ derivatives

Calculating the partial derivatives of Eq. (1) with respect to depth H and fractional cover B yields (omitting the wavelength dependence for the sake of clarity)

$$\frac{\partial\mu}{\partial H} = r_{r,s,\infty} (k_d + k_u^c) e^{-(k_d+k_u^c)H} - \frac{1}{\pi} [B\rho_{b,1} + (1-B)\rho_{b,2}] (k_d + k_u^b) e^{-(k_d+k_u^b)H} \quad (15)$$

$$\frac{\partial\mu}{\partial B} = \frac{1}{\pi} [\rho_{b,1} - \rho_{b,2}] e^{-(k_d+k_u^b)H} \quad (16)$$

where $r_{r,s,\infty}$ is the deep water reflectance, k_d , k_u^c and k_u^b are the attenuation coefficients, and $\rho_{b,1}$ and $\rho_{b,2}$ are two substratum albedos.

The partial derivatives of Eq. (1) with respect to phytoplankton and CDOM absorption coefficients at 440 nm, $a_\phi(440)$ and $a_g(440)$, respectively, and particle backscattering coefficient at 550 nm, $b_{bp}(550)$, (hereafter denoted, respectively, P , G and X for the sake of brevity [14, 17]) are

calculated similarly for these three parameters. In the case of P , it is given by

$$\begin{aligned} \frac{\partial \mu}{\partial P} = & \frac{\partial r_{rs,\infty}}{\partial P} \left(1 - e^{-(k_d+k_u^c)H} \right) + r_{rs,\infty} \left(\frac{\partial k_d}{\partial P} + \frac{\partial k_u^c}{\partial P} \right) H e^{-(k_d+k_u^c)H} \\ & - \frac{1}{\pi} [B\rho_{b,1} + (1-B)\rho_{b,2}] \left(\frac{\partial k_d}{\partial P} + \frac{\partial k_u^b}{\partial P} \right) H e^{-(k_d+k_u^b)H}. \end{aligned} \quad (17)$$

Defining $\kappa = a + b_b$ and $u = b_b/(a + b_b)$ with a and b_b the total absorption and backscattering coefficients, respectively, Eq. (17) requires us to calculate the derivatives of Eq. (2) to Eq. (5):

$$\frac{\partial r_{rs,\infty}}{\partial P} = (0.084 + 0.34u) \frac{\partial u}{\partial P} \quad (18)$$

$$\frac{\partial k_d}{\partial P} = \frac{1}{\cos \theta_s} \frac{\partial \kappa}{\partial P} \quad (19)$$

$$\frac{\partial k_u^c}{\partial P} = \frac{1.03}{\cos \theta_v} \left[\frac{\partial \kappa}{\partial P} (1 + 2.4u)^{0.5} + 1.2\kappa \frac{\partial u}{\partial P} (1 + 2.4u)^{-0.5} \right] \quad (20)$$

$$\frac{\partial k_u^b}{\partial P} = \frac{1.04}{\cos \theta_v} \left[\frac{\partial \kappa}{\partial P} (1 + 5.4u)^{0.5} + 2.7\kappa \frac{\partial u}{\partial P} (1 + 5.4u)^{-0.5} \right]. \quad (21)$$

Equations (18)-(21) also require us to calculate the derivatives of κ and u :

$$\frac{\partial \kappa}{\partial P} = \frac{\partial a}{\partial P} + \frac{\partial b_b}{\partial P} \quad (22)$$

$$\frac{\partial u}{\partial P} = \frac{a \frac{\partial b_b}{\partial P} - b_b \frac{\partial a}{\partial P}}{(a + b_b)^2}. \quad (23)$$

Since b_b does not depend on P (Eq. (7)), we have $\partial b_b/\partial P = 0$. The last derivative is given by

$$\frac{\partial a}{\partial P} = a_0 + a_1(1 + \ln P). \quad (24)$$

Equations (18)-(24) thus make it possible to calculate Eq. (17). Similarly to $\partial \mu/\partial P$, $\partial \mu/\partial G$ and $\partial \mu/\partial X$ can be derived using

$$\frac{\partial a}{\partial G} = a_g^* \quad (25)$$

$$\frac{\partial b_b}{\partial X} = b_{bp}^* \quad (26)$$

the remaining derivatives $\partial b_b/\partial G$ and $\partial a/\partial X$ being zero. Equations (15)-(26) fully determine $\mathbf{I}_F(\Delta)$ (Eq. (12)) and thus $\mathbf{CRB}(\Delta) = \mathbf{I}_F(\Delta)^{-1}$.

Funding

Direction Générale de l'Armement (DGA) (project # ANR-15-ASTR-0019).

Acknowledgments

We would like to thank the Oregon State University, College of Earth, Ocean, and Atmospheric Sciences for providing us the atmospherically-corrected HICO image, Christophe Lerebourg for his help with satellite data processing, Timothy Kendall for checking the English, and the two anonymous reviewers for their valuable comments and suggestions.